The Oxford 3D Thermophysical Model with application to PROSPECT/Luna 27 Study Landing Sites

(1, now at 2) Oliver King, (1) Tristram Warren (1) Neil Bowles, (3) Elliot Sefton-Nash, (3) Richard Fisackerly, (3) Roland Trautner.

[1] Atmospheric, Oceanic and Planetary Physics Department, University of Oxford, Oxford, United Kingdom (tristram.warren@physics.ox.ac.uk, neil.bowles@physics.ox.ac.uk).

[2] Department of Physics & Astronomy, University of Leicester, University Road, Leicester, LE1 7RH, UK (ortk1@leicester.ac.uk)

[3] ESTEC, European Space Agency, Keplerlaan 1, Noordwijk 2201AZ, Netherlands (e.sefton-nash@cosmos.esa.int, richard.fisackerly@esa.int roland.Trautner@esa.int)

Corresponding author: Oliver King and Tristram Warren

Abstract

A 3D thermal model that includes a discrete subsurface exponential density profile, surface shadowing and scattering effects has been developed to simulate surface and subsurface temperatures across the Moon. Comparisons of the modelled surface temperatures with the Lunar Reconnaissance Orbiter's Diviner Lunar Radiometer Experiment ("Diviner") measured temperatures show significant improvements in model accuracy from the inclusion of shadowing and scattering effects, with model errors reduced from ~10 K to ~2 K for mid-latitude craters. The 3D thermal model is used to investigate ice stability at potential landing sites near the lunar south pole, studied for Roscosmos' 'Luna Resource' (Luna 27) lander mission on which the ESA PROSPECT payload is planned to fly. Water ice is assumed to be stable for long periods of time (> 1 Gyr) if temperatures remain below 112 K over diurnal and seasonal cycles. Simulations suggest ice can be stable at the surface in regions near to potential landing sites in permanently shaded regions and can be stable below the surface in partly shaded regions such as pole-facing slopes. The simulated minimum constant subsurface temperature (where the seasonal temperature cycle is attenuated) typically occurs at a depth of ~50 cm and therefore the minimum depth where ice can be stable is $0 \leq z \lesssim 50cm$.

1 Introduction

Thermal models based on finite difference methods can be used to simulate the heat transport and therefore the temperature environment of the lunar regolith – the layer of granular material that covers the lunar surface produced by the cumulative effect of impacts and other surface processes over geologic time. The 1D thermal diffusion equation can be solved using assumed regolith properties and conditions to calculate the evolution of the lunar surface and sub-surface temperature over time.

Lunar surface temperatures are inferred by remote sensing measurements made by the Lunar Reconnaissance Orbiter Diviner Lunar Radiometer Experiment ("Diviner"), which observes infrared radiance from the lunar surface in 4 broadband thermal channels. These remotely-sensed temperatures are important for thermal model validation and are used to infer lunar surface properties. Retrieval of regolith parameters is achieved by inverting a thermal model for parameter values that result in best fit between model and measured temperatures (Paige et al, 2010a). For example, the near-surface density affects the thermal inertia[1] of the surface, leading to different heating and cooling rates for different densities (Hayne et al, 2017).

Sub-surface temperature profiles are difficult to remotely measure, so thermal models are crucial for understanding the temperature environment in the top ~1 m of the lunar surface, where diurnal and seasonal thermal signals dominate. Of particular importance is the role of these signals with respect to permanently or temporarily shadowed terrain in polar regions, due to evidence for the presence of sub-surface volatiles and the dependence of volatile stability on sub-surface temperature (Paige et al, 2010b, Paige et al, 2010a).

The Chinese Chang'E 1 and 2 microware radiometer (MRM) instruments have both taken global measurements of the lunar surface from lunar orbit. Both instruments were identical and observed the Moon in four different channels at 3.0, 7.8, 19 and 37 GHz (~ 10, 7, 1.5 and 0.8 cm). For average

[1] Thermal inertia, $\mathrm{I} = \sqrt{K\rho c_p}$, quantifies the resistance of the lunar surface to temperature changes (Hayne et al, 2017).

regolith densities found across the Moon those channels will be sensitive to sub-surface temperatures down to depths of ~10x the observation wavelength. The Chang'E MRM instruments therefore potentially offer a way of remotely sensing the sub-surface temperatures across the lunar surface. However, interpreting the MRM dataset is complex. Sub-surface temperature profiles retrieved using the MRM observations can be degenerate with composition and density. The MRM data is also at lower spatial resolution than the Diviner observations used in this study (2 Km compared to 30 Km) (Siegler and Feng, 2017, Wang et al, 2010, Wei et al, 2016).

After consideration of these two complications, this study did not attempt to use the Chang'E MRM datasets to constrain the modelled sub-surface temperature profile. The Chang'E MRM dataset does have potential for additional measurement constraint of sub-surface temperature and so will be a useful additional data source for future comparisons between thermal models such as the one described in this study.

In this study, water ice is assumed to be stable for regions where the temperature remains <112 K throughout the diurnal and seasonal cycles, implying a sublimation rate <1 kg m^{-2} Gyr^{-1}(Paige et al, 1992). The exact value of 112 K is not a unique indication of ice stability, as the presence of ice is dependent on the history of deposition and subsequent subsurface migration of the ice, leading to a range of temperatures below which ice may be located at the current time (Schorghofer and Taylor, 2007, Zhang and Paige, 2009). However, a discrete value of 112 K is useful in this study to allow simple classification of areas where ice can and cannot be stable for very long periods (~Gyr).

This simple thermal modelling with a cut off of 112 K, cannot be used to positively determine the existence of all water ice locations on the moon (as water ice will not exist everywhere it can possibly be stable) but can be used to identify the limited areas where water ice may be present and what approximate depth.

Examples of existing surface thermal models with differing levels of complexity include the Paige (Paige et al, 2010b), Vasavada (Vasavada et al, 2012) and heat1d (Hayne et al, 2017) thermal models.

77 The Paige model simulates the lunar regolith as two discrete layers, with a lower density layer near
78 the surface and a higher density layer below. It is a 3D thermophysical model, so simulates regions of
79 the lunar surface, accounting for terrain blocking solar radiation and radiation between the model's
80 surface elements (because of the surface elements' thermal emission and scattering of radiation)[2].

81 The Vasavada thermal model (Vasavada et al, 2012) introduced a continuously increasing sub-surface
82 regolith density profile. This density profile produces modelled temperatures which are a significantly
83 better match to Diviner temperature measurements than a two-layer density profile, especially
84 around sunrise and sunset when the temperature changes rapidly.

85 The heat1d thermal model (Hayne et al, 2017) is a 1D model, so treats each surface element
86 independently and does not account for any 3D effects from the surface element's environment. It
87 uses a continuous density profile, based on the profile introduced by Vasavada et al (2012), with
88 density increasing with depth z as

89 $$\rho(z) = \rho_d - (\rho_d - \rho_s)e^{-\frac{z}{H}}$$

90 *Equation 1*

91 where the H parameter is the scale height of density variations, ρ_s is the density at the surface ($z =$
92 0) and ρ_d is the density at large depths ($z \gg H$). See Figure 1 for typical density profiles produced by
93 Equation 1.

[2] In this study, the blocking of solar flux is referred to as “shadowing”, the radiation from other surface elements is collectively referred to as “scattering”. Shadowing and scattering are collectively referred to as “3D effects”.

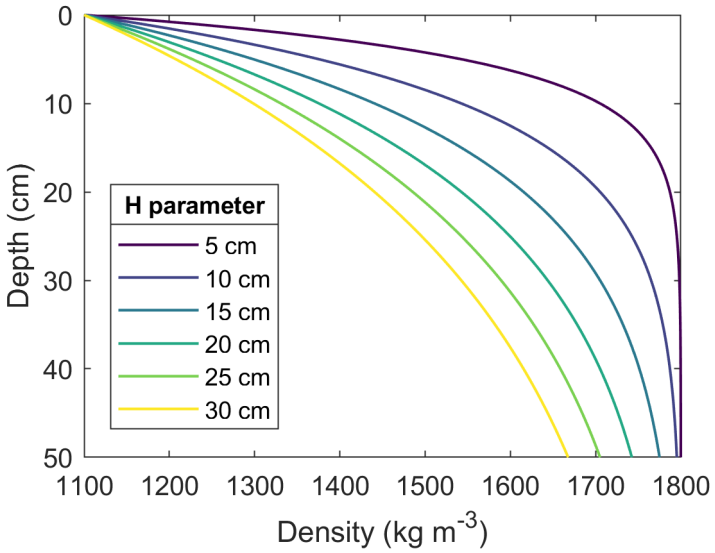

Figure 1: heat1d model (Hayne et al, 2017) density profiles for the top 50cm of the lunar regolith for different values of the H parameter (the vertical density scale height given in Equation 1) with ρ_s=1100 kg/m^3 and ρ_d=1800kg/m^3.

The heat capacity and conductivity of the lunar surface depend on the local density, so are functions of H (Hayne et al, 2017, Fountain and West, 1970). This makes the parameter H important in modelling how fast the lunar surface cools at night and hence the minimum temperature of the surface.

The 3D thermal model developed in this study (the Oxford 3D thermophysical model, O3DTM) combines the 1D sub-surface heat flow from the heat1d model (Hayne et al, 2017) and the 3D shadowing and scattering effects used in the Paige and Vasavada model (Paige et al, 2010b) for the first time. Validation of O3DTM has been completed by comparing modelled surface temperatures to bolometric temperatures observed by Diviner (see section 4.1). The same surface regions were also simulated using the heat1d thermal model to compare the 1D and a 3D thermophysical model approach.

After ground testing, the O3DTM has been used to assess the potential for water ice stability at eight south polar study landing sites for the Roscosmos Luna 27, “Luna Resurs”, lander. The PROSPECT instrument package is currently being developed by the European Space Agency (ESA) for flight on Luna 27 and to investigate potential in situ near-surface volatiles that might be present in the lunar polar regions. Launch is scheduled for the early 2020s (Trautner et al 2018, Sefton-Nash et al 2018). PROSPECT will consist of a drill (ProSEED) that will collect samples from the regolith at depths of up to

1 m below the lunar surface and transfer them into a miniaturised chemical laboratory (ProSPA), where samples will be heated to 1000° C in the presence of different reagent gases to extract a range of different volatile species, including water.

The eight study landing sites used in this study have been provided by ESA, identified as specific study sites for Luna 27. We have performed simulations using O3DTM of the thermal environment over spatial domains that extend up to ±10° latitude and ±5° longitude from each site, at a variety of resolutions (from 4 to 128 pixels per degree). In section 6 we report in detail the results from the simulation of landing site number 8 as a case study (see https://github.com/tw7044/O3DTM.git where all simulations can be downloaded). Finally, in section 8 we map the depth at which water ice would be expected to be stable across landing site 8.

2 Datasets

This study uses data from two instruments onboard the Lunar Reconnaissance Orbiter (LRO). Elevation and albedo Gridded Data Records (GDRs) are from the Lunar Orbiter Laser Altimeter (LOLA) experiment (Smith et al, 2010) and GDRs of surface bolometric temperature are from the Diviner Lunar Radiometer Experiment (Paige et al, 2010a).

The modelled simulations were at resolutions of 4, 16 and 128 ppd (pixels-per-degree). For convenience and comparability with non-polar model runs, input data was sourced from cylindrical projection GDRs. The highest spatial resolution LOLA albedo dataset providing global coverage available to download from NASA's Planetary Data System (PDS) is 8 ppd, so the albedo was inferred by fitting to the maximum Diviner temperatures (see section 5).

Diviner GDRs of bolometric brightness temperature (T_{BOL}) are the best available estimate of surface kinetic temperature and are calculated by spectrally integrating radiance and fitting to a Planck curve. GDRs of T_{BOL} used in this study were downloaded from the PDS, and cover over 6 years of surface temperature measurements, from July 2009 to November 2015, providing surface temperatures for

each gridded surface element at a wide range of local times. This means extreme temperatures, that normally occur at midday (maximum) and just prior to sun rise (minimum) are recorded. These extreme temperatures are important for fitting parameters in the model, such as H, albedo and emissivity (see section 5).

The LOLA albedo measurements are performed by a 1064.4 nm laser (Smith et al, 2010), so are scaled to the broadband solar albedo value using the method described in (Hayne et al, 2017). LOLA albedo measurements have the advantage of being based on zero phase angle measurements over the entire lunar surface, so artefacts introduced by increased shadowing at high latitudes are removed.

Ephemeris data downloaded from JPL Horizons were used for modelling the lunar rotation and seasonal variation. Additional lunar parameters are taken from (Hayne et al, 2017) and are given in section 13.1.

3 Thermal model description

The thermal model developed in this study consists of a 1D subsurface model coupled with a 3D radiative transfer model which together simulate the surface and subsurface temperatures of any region on the lunar surface. The model divides a surface that is to be modelled into a grid of surface elements and each element contains discrete subsurface layers at increasing depths from the lunar surface.

3.1 1D sub-surface model

Below the surface, only vertical heat conduction is considered, meaning that the subsurface behaviour of each surface element is independent of the other surface elements. The surface elements are several hundred metres across (limited by the resolution of the 128ppd LRO datasets), which is much

larger than the temperature scale lengths[3] in lunar regolith (z_s< 1 m), so any horizontal subsurface heat flux can be neglected.

The heat1d model (Hayne et al, 2017) is used to model subsurface heat flux in this study. It typically uses 26 layers in the top 2.5 m of the lunar surface and numerically simulates their temperatures at discrete time steps for a given set of surface parameters. A full list of variable names, the model parameters and their default values are given in Appendix 13.1.

The temperature variation of a layer at depth z below the lunar surface at time t is modelled using the one-dimensional heat equation, Equation 2:

$$\rho c_p \frac{\partial T}{\partial t} = \frac{\partial}{\partial z}\left(K \frac{\partial T}{\partial z}\right)$$

Equation 2

where T is temperature and ρ is density. The specific heat capacity c_p is a function of T and the thermal conductivity K is a function of T and ρ (Hayne et al, 2017). See Appendix 13.1 for functional forms of K and c_p. Equation 2 is used to model the conduction between the model subsurface layers. The bottom boundary condition accounts for the internal heat flux of the moon, $Q_{int} = 0.018\ Wm^{-2}$ (Langseth et al, 1976) and the surface boundary condition accounts for incident flux and thermal emission.

Temperature gradients decrease with depth, i.e. the largest temperature gradients occur near the surface, to capture this in the model the thickness of the model subsurface layers increases with depth below the lunar surface. This ensures the sharp temperature gradients (~2 K/μm) are captured adequately whilst also minimising the total number of model layers (as simulation time scales approximately linearly with number of layers).

[3] The thermal skin depth, $z_s = \sqrt{\frac{KP}{\rho c_p \pi}}$, is the depth where temperature variations with a period P are damped by a factor of e (Carslaw and Jaeger, 1959).

In this study, simulations are run to a depth of 2.65 m, as diurnal and seasonal variations are completely damped at this depth. A typical simulation (with default parameter values given in section 13.1) to 2.65 m depth has 26 layers, 20 of which are in the top 1m of the regolith.

For a more detailed discussion of the heat1d model, see the Appendix in Hayne et al (2017).

3.1.1 Temperature initialisation

The heat1d model initial temperature profile is an exponential decay between the temperature at the surface T_0 and the temperature at large depths T_N where the temperature at depth z is given by

$$T(z) = T_N - (T_N - T_0)e^{-\frac{z}{H}}$$

and T_0 is found by calculating instantaneous thermal equilibrium with incoming solar radiation and $T_N = T_0/\sqrt{2}$.

After the temperature initialisation, the heat1d model is run for 5 years to allow the temperatures to stabilise over several diurnal and seasonal cycles:

1. Initialise all layer temperatures.
2. Run model for (5 year) stabilisation period.
3. Run model for (~5 year) period overlapping Diviner data to produce results.

This stabilisation period is sufficient to remove any effects of the temperature initialisation on the model output temperatures for simulations which are run to depths $\lesssim 1m$. However, for simulations > 1 m this temperature initialisation was found to be inadequate to quickly initialise the temperature profile. Simulations to the depth of 2.65 m used in this study would require a stabilisation time of > 50 years to completely remove the influence of the temperature initialisation. This would be unfeasibly long, so a new temperature initialisation routine was developed to allow faster simulations of larger depths.

The new routine initially runs the model for a shallow depth, then progressively adds model layers to increase the simulation depth. This provides a more accurate estimate (first guess) to the subsurface temperature, and hence allows for a faster initialisation of the model. The new model sequence is as follows:

1. Initialise temperatures of top layers, down to depth of 2 diurnal thermal skin depths (≈20cm)
2. Run model for 1 year to allow temperature of top layers to stabilise over a seasonal cycle.
3. Run model for 3 years, progressively adding deeper layers at equal intervals (one new layer added every 3 months).
4. Run model for 5 years to allow temperature profile (with all layers) to fully stabilise over multiple seasonal cycles.
5. Run model for (~5 year) period overlapping Diviner data to produce results.

This technique allows significantly faster simulations of temperatures at large depths, only requiring 9 years to initialise and stabilise the temperature profile. The new technique was tested by using different temperature initialisations (varying from 50K to 350K at large depths) which all produce the same final output temperature profiles (see Figure 2).

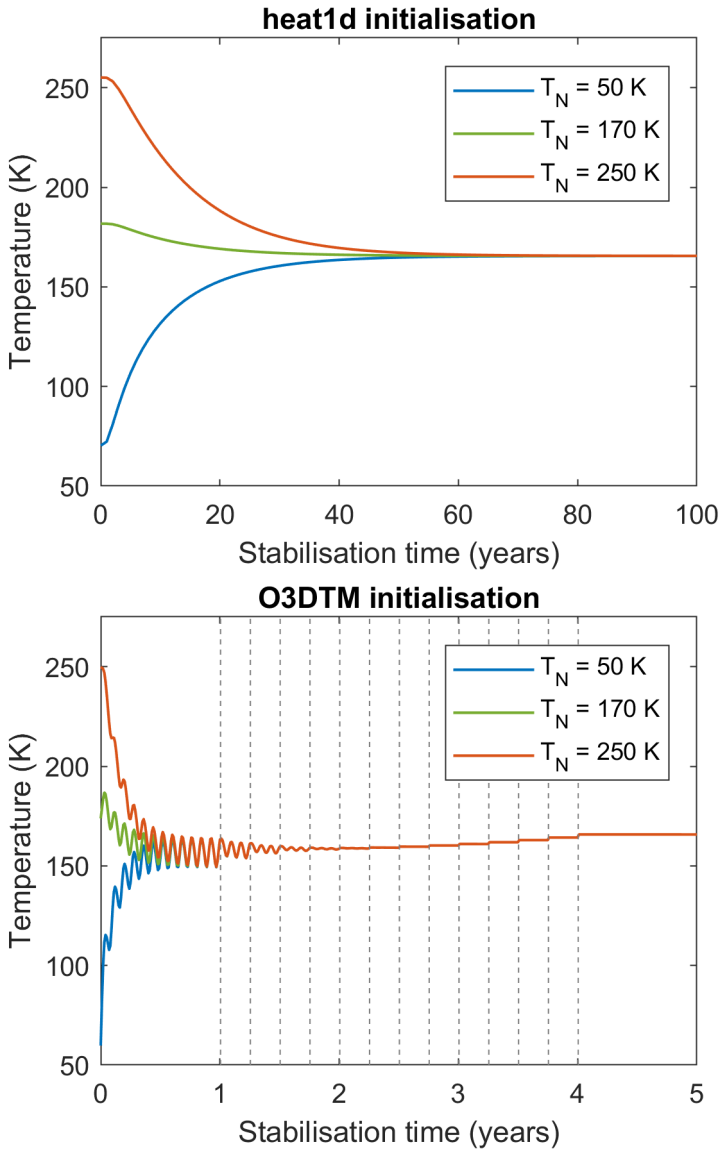

Figure 2: Temperature of deepest model layer (2.65m) using different values for T_N in the heat1d model temperature initialisation process (at a latitude of 80˚) and the deepest simulated layer with our new initialisation process. 50 K is representative of a shadowed area, 170 K for a flat area and 250 K for a sun-facing slope. The heat1d model initialisation process requires 60 years for the different initialisation temperatures to be consistent to 1 K while our new routine is consistent to < 0.01 K in only 9 years. The vertical dashed lines show when model layers are added in the new initialisation, increasing the simulated depth and therefore decreasing the size the diurnal temperature oscillations occurring in the bottom modelled layer.

The simulated period covers about 15 years of simulation time, corresponding to real lunar conditions (using ephemeris data from JPL Horizons) from 2000 to 2015. The simulation begins at midday local lunar time in January or February 2000 (the exact date depends on the longitude of the simulated area).

3.2 3D radiative transfer

The surface boundary condition for each surface element takes the form

$$\bar{\varepsilon}\sigma T^4 = K\frac{\partial T}{\partial z}\Big|_{z=0} + Q_{abs}$$

Equation 3

which balances the grey body thermal emission from the surface ($\bar{\varepsilon}\sigma T^4$) against the heat flux from subsurface layers ($K\frac{\partial T}{\partial z}\Big|_{z=0}$) and the absorbed flux incidence on the surface (Q_{abs}). The absorbed flux includes contributions from the visible solar irradiation directly incident on the surface plus visible radiation scattered from other surfaces (including multiple scatterings) and infrared thermal radiation emitted from other surfaces.

Scattering calculations are performed by calculating matrices of flux coefficients $C_{ij}^{vis}$and C_{ij}^{IR}. C_{ij}^{vis} represents the fractions of direct solar radiation scattered from surface element i and absorbed by surface element j. C_{ij}^{IR} represents the fraction of infrared radiation emitted by surface element i and absorbed by element j. These coefficients give the total flux absorbed by surface element j in a given time step as

$$Q_j^{abs} = Q_{\odot j} + \sum_i (C_{ij}^{IR} Q_i^{IR} + C_{ij}^{vis} Q_i^{vis})$$

where $Q_{\odot j}$ is the direct solar flux absorbed by j, $Q_i^{IR} = \bar{\varepsilon}\sigma T_i^4$ is the grey body thermal emission from i and Q_i^{vis} is the solar radiation directly scattered by i.

The direct solar flux absorbed by a surface element is given by

$$Q_\odot = F_\odot\big(1 - A(\theta)\big)\cos\theta$$

where θ is the angle to the surface normal and $F_\odot$ is the solar flux which has been taken to be $1361 Wm^{-2}$ when the sun is visible, consistent with the heat1d model. The albedo of the surface ($A(\theta)$) is dependent on the incident (angle between the incoming sun light and the surface normal) angle of the solar illumination. In this model as in the heat1d model, the albedo of the surface for a ray at a given incidence angle is parametrised as

$$A(\theta) = A_0 + a\left(\frac{\theta}{\pi/4}\right)^3 + b\left(\frac{\theta}{\pi/2}\right)^8$$

Equation 4

where a and b are constants (Keihm, 1984), given in section 13.1. For computational efficiency, the sun is simulated as a point source of radiation. The approximation of the sun as a point source allows faster simulations, at the cost of slightly reduced model accuracy. This reduction in accuracy is mainly confined to times around sunrise and sunset where the point source approximation causes a step change in incident flux rather than the smooth change in flux from an extended source.

The C_{ij} coefficients are calculated by ray tracing between the centres of each pair of surface elements and incorporate the angular dependence of albedo (Equation 4) for visible scattering. The coefficients account for all possible paths for the radiation through the simulated area, including via multiple scatterings. The model, therefore, accounts for an infinite number of scatterings from the lunar surface by tracing a ray from facet to facet until it leaves the surface. $C_{ij} = 0$ for surface elements which have no line of sight and no indirect lines of sight via multiple scatterings. Surface elements are assumed to be flat for scattering and shadowing calculations. For a more detailed discussion of the calculation of these coefficients, see 13.2.

This model does not include azimuth angle[4] effects on scattering, meaning the C_{ij} coefficients are constant with time. This allows the coefficients to be pre-calculated in the simulation and the flux calculation to be performed rapidly as simple matrix multiplications at each time step. The intensity of scattered radiation has been shown to be dependent on azimuth angle and is described more fully by a bidirectional reflectance distribution function (Foote et al, 2009, Pommerol et al, 2011, Warren et al, 2017, Warren et al, 2019). The inclusion of bidirectional reflectance functions would improve the model accuracy in non-flat areas, by more accurately simulating the scattering of radiation. However, the inclusion of bidirectional reflectance would require the values of C_{ij}^{vis} to be calculated

[4] The azimuth angle is the angle between the projections of the incident and reflected rays onto the surface.

at each time step due to the changing solar angle, significantly slowing the scattering calculations. It was therefore decided the inclusion of full bidirectional reflectance would make the simulation too slow with the computing power and time available for this study.

Additional less significant effects from sources of radiation, such as 'earthshine' (radiation from the earth) and stellar flux (from stars other than the Sun) are not accounted for in this model. This will slightly reduce the accuracy of the modelled absorbed flux, though the magnitude of this error will be small, especially at the polar latitudes used in this study where the Earth is low on the horizon.

4 Effect of inclusion of 3D thermal transfer on temperature estimates

The addition of 3D effects was found to have a large effect on crater temperatures. The addition of shadowing reduces the maximum temperature of permanently shaded craters by >150 K. Including scattering was found to increase the maximum temperature of small craters by ~10 K at the equator, rising with latitude to >100 K for permanently shaded regions at the lunar poles. The temperatures of flat surfaces are unaffected by including scattering, due to the absence of lines of sight between surface elements (Figure 3). Minimum temperatures were found to be similarly affected by 3D effects, with the magnitude of changes in minimum temperature being about a quarter of the magnitude of changes in crater maximum temperatures.

The scattered radiation absorbed by each surface element is roughly constant over the crater and varies significantly less than the solar radiation absorbed by each surface element. Therefore, the temperature difference between the 3D and 1D models is larger in regions where the incident solar flux is lower, as scattered radiation is a more dominant heat source in these regions. This is seen in simulations of mid-latitude craters where the north facing crater wall (for northern hemisphere craters) has a larger temperature difference between the 1D and 3D models than the south facing crater wall.

4.1 Comparison to Diviner temperatures

The addition of scattering was found to significantly improve the accuracy of simulated crater temperatures when compared to the measured Diviner temperatures. Figure 3 shows the model surface temperature error for a typical equatorial crater. Here we define model error as the difference between the bolometric maximum surface temperature measured by Diviner, and the modelled surface temperature corresponding to the time of the Diviner maximum temperature measurement. Figure 3 shows that errors in the base of the equatorial crater maximum temperatures are reduced from ~-10 K with the 1D model to ~-2 K with the 3D model, which is small enough to be accounted for by parameter variation across the lunar surface.

The simulated temperatures of east facing crater walls in these small craters are generally too cold in both the 1D and 3D models. These crater walls are well illuminated at sunrise and early in the lunar day but have less illumination by midday (when the maximum temperatures generally occur). Therefore, this error is likely due to a combination of incorrect parameters (such as density, thermal conductivity or the H parameter) reducing the thermal inertia of the surface and causing these areas to cool too quickly in the model and therefore have lower temperatures.

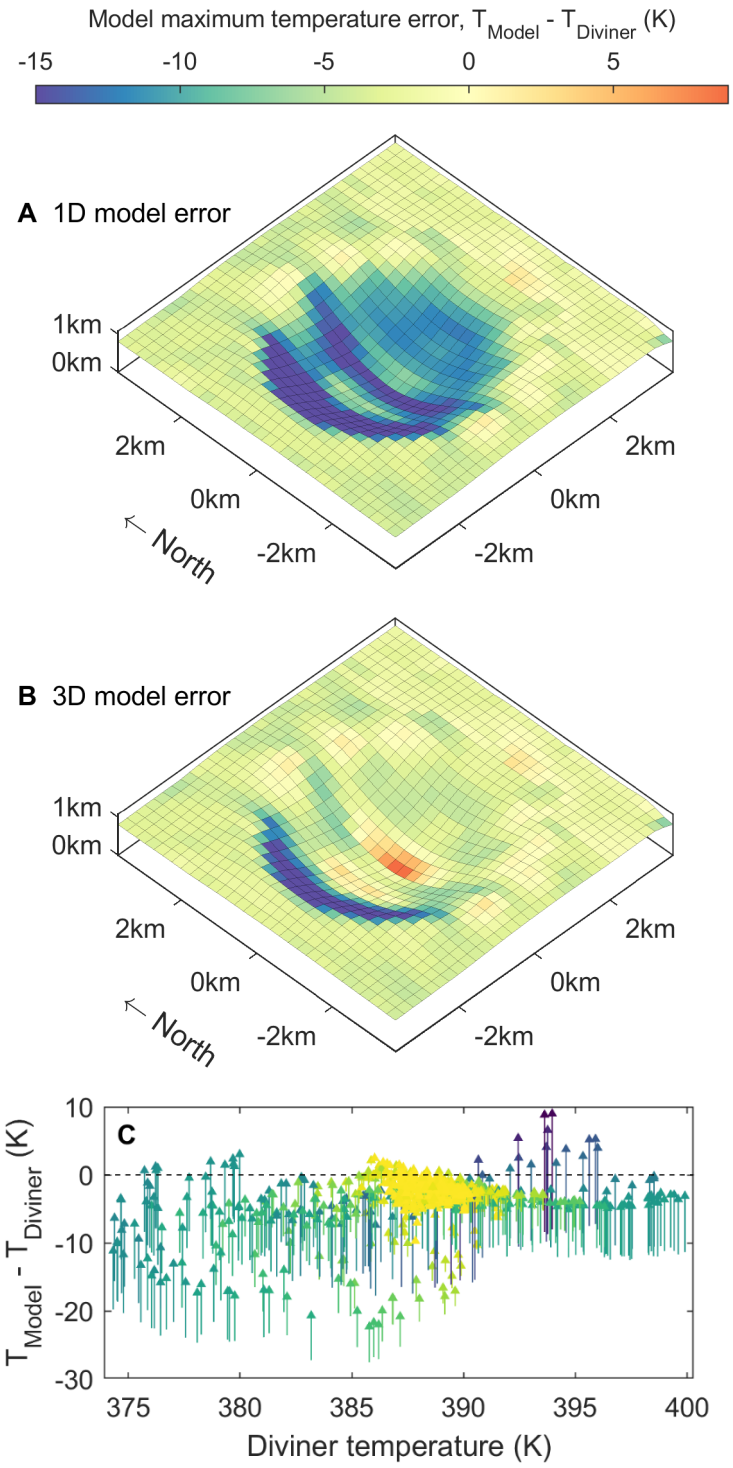

*Figure 3: 3D model improvements in simulated maximum temperatures for 'Blagg' crater (at 1.2°N). **A** and **B** show the differences in modelled temperatures and measured diviner temperatures for the 1D and 3D models respectively. **C** shows the change in temperature error for each surface element as an arrow starting at the 1D model error and ending at the 3D model error. Arrows are coloured by their length (i.e. difference between 1D and 3D model temperatures); the yellow arrows represent the surface elements on the surface surrounding the crater which have negligible temperature changes between the 1D and 3D models.*

5 Parameter fitting

Diviner temperatures are used to infer the bond albedo A_0 and H parameter across the lunar surface for each surface element within the simulation environments. Measured maximum and minimum Diviner temperatures for each surface element are compared to modelled surface temperatures with a range of parameters to estimate the value of the parameter consistent with the Diviner temperature. The sensitivities in Figure 4 show that surface bond albedo (A_0 in Equation 4) is very dependent on the maximum (midday) surface temperature, but has little effect on the minimum surface temperature experienced just prior to sunrise. The H parameter, however, is very dependent on the minimum temperature and has little effect on the maximum temperature. Given these sensitivities, the bond albedo should be fitted by comparing the maximum simulated temperatures to the maximum surface temperatures measured by Diviner and the H parameter should be fitted by comparing the minimum temperatures. The use of the maximum and minimum temperatures for fitting reduces the effect of the degeneracy between the bond albedo and H parameter which is more significant at intermediate temperatures.

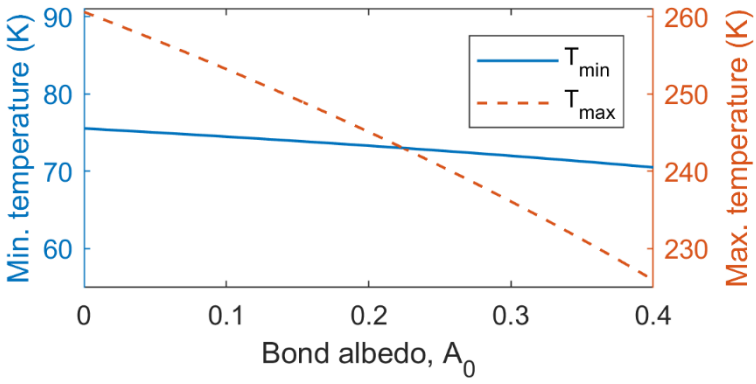

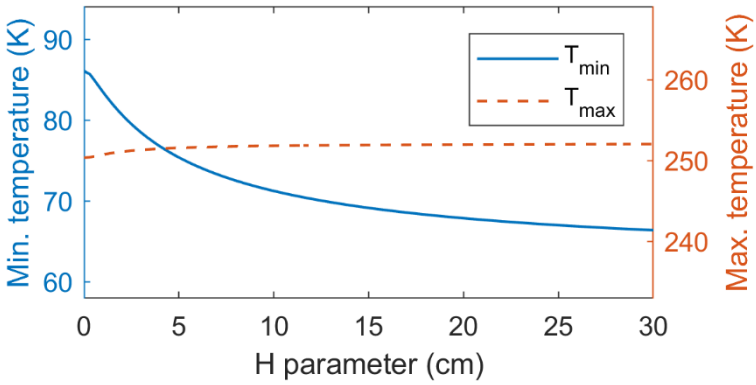

Figure 4: Effect of bond albedo A_0 and H parameter variation on typical modelled maximum and minimum temperatures. The temperatures shown here correspond to a point at a latitude of 80° with no slope and all other parameters held constant. The exact relationship between A_0, H & T will vary for each surface element, depending on its latitude, slope and environment.

The parameter fitting routine used in this study to fit the bond albedo and H parameter was:

1. Run the 3D thermal model with initial parameter guess (e.g. $A_0 = 0.12$ for every surface element) to generate initial model surface temperatures T_{model}.
2. For each surface element, compare T_{model} with the corresponding Diviner temperature $T_{Diviner}$ to choose a new parameter value for this surface element (e.g. if $T_{model} < T_{Diviner}$ then the new albedo value for this surface element is $A_0 = 0$).
3. Run the 3D thermal model with the new parameter values to produce new values for T_{model}.

4. For each surface element, perform a linear interpolation with the two previous parameter values and their associated T_{model} values to find a new parameter value consistent with $T_{Diviner}$.
5. Repeatedly run the 3D thermal model with new interpolated parameter values to allow the parameter values for each surface element to converge and stabilise.

This routine quickly converges on parameter values, requiring only 5 iterations of running the thermal model. The routine produces parameter fittings which account for the simulation environment, such as with higher albedo values for one surface element slightly increasing the temperature of nearby surface elements due to the increased flux scattered from this surface element.

6 Case study sites

The model was used to investigate eight study landing sites near the lunar south pole; with the coordinates of each of the simulated landing sites given in Table 1 and mapped in Figure 5. The landing sites were simulated at three different resolutions (4 ppd, 16 ppd and 128 ppd). Each model simulation was kept to ~2 hours in length by adapting the size of the simulated area. The size of the simulated area varied from ~245 km for the 4 ppd resolution simulations to ~9 km for the 128 ppd resolution simulations, full details are given in Table 1 and Table 2. The different simulation resolutions and area lengths are given in Table 2 and shown graphical in Figure 6. In this paper site 8 has been chosen for more detailed study.

Site	Latitude	Longitude
1	-79.30	-56.00
2	-80.56	-37.10
3	-81.24	68.99
4	-81.35	22.80
5	-84.25	-4.65
6	-84.33	33.19
7	-85.33	-4.78
8 *	-82.70	33.50

Table 1: Landing sites analysed with thermal model. Latitudes and longitudes are degrees North and East respectively.

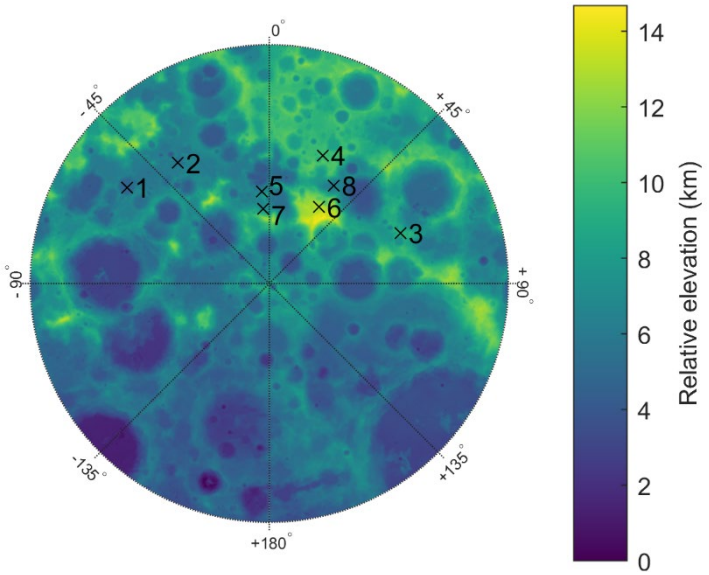

Figure 5: Map of landing sites, centred on the lunar south pole and extending to 75°S. All landing sites are on the near side of the moon. The colour scale shows LOLA elevation data.

Resolution	Latitude buffer	Longitude buffer	Simulation size	Surface element size
4ppd	4.00°	20.00°	~ 245 km	~ 8 km
16ppd	2.00°	10.00°	~ 122 km	~ 2 km
128ppd	0.15°	0.75°	~ 9 km	~ 230 m

Table 2: Landing site simulation resolutions. The resolution gives the number of pixels per degree of latitude. The latitude and longitude buffers give the distance from the landing site that is simulated at each resolution (e.g. Landing Site 1 at 16ppd simulates longitudes from -46° to -66°)). The sizes given are the North-South lengths of the whole simulation environment and each surface element.

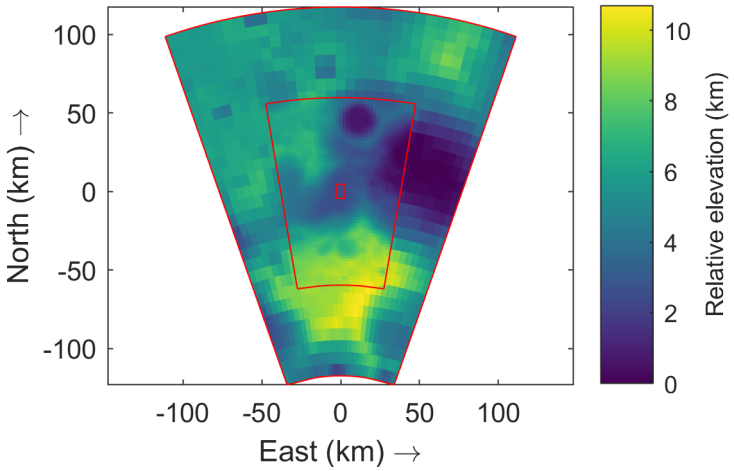

Figure 6: Map of different landing site resolutions for Landing Site 8. The red boxes from largest to smallest are 4ppd, 16ppd and 128ppd.

The simulation grids are based on the cylindrical projection used for LOLA and Diviner elevation and temperature datasets, allowing for easy direct comparison between modelled and measured surface temperatures. At polar latitudes, the East-West spatial resolution of this grid (surface elements per

385 metre) is significantly higher than the North-South spatial resolution, as one degree of longitude
386 corresponds to a much smaller physical distance than one degree of latitude at high latitudes (by a
387 factor of $\cos\phi$, where $\phi \sim 90°$ is the latitude). Therefore, the grids used in the simulations are
388 compressed in along the East-West direction to produce a surface element grid which has
389 approximately equal East-West and North-South spatial resolution[5].

390 The 16ppd wide resolution was generally used for more detailed analysis as it provided a balance
391 between simulating the local small-scale variations of the lunar surface and simulating a large enough
392 area to account for shadowing and re-radiation effects.

[5] Compression is performed by taking the mean of the elevation values for every $n \sim \Delta_{NS}/\Delta_{EW}$ surface elements in the uncompressed site where Δ_{NS} is the surface element size in the North-South direction and Δ_{EW} is the uncompressed surface element size in the East-West direction and n is an integer.

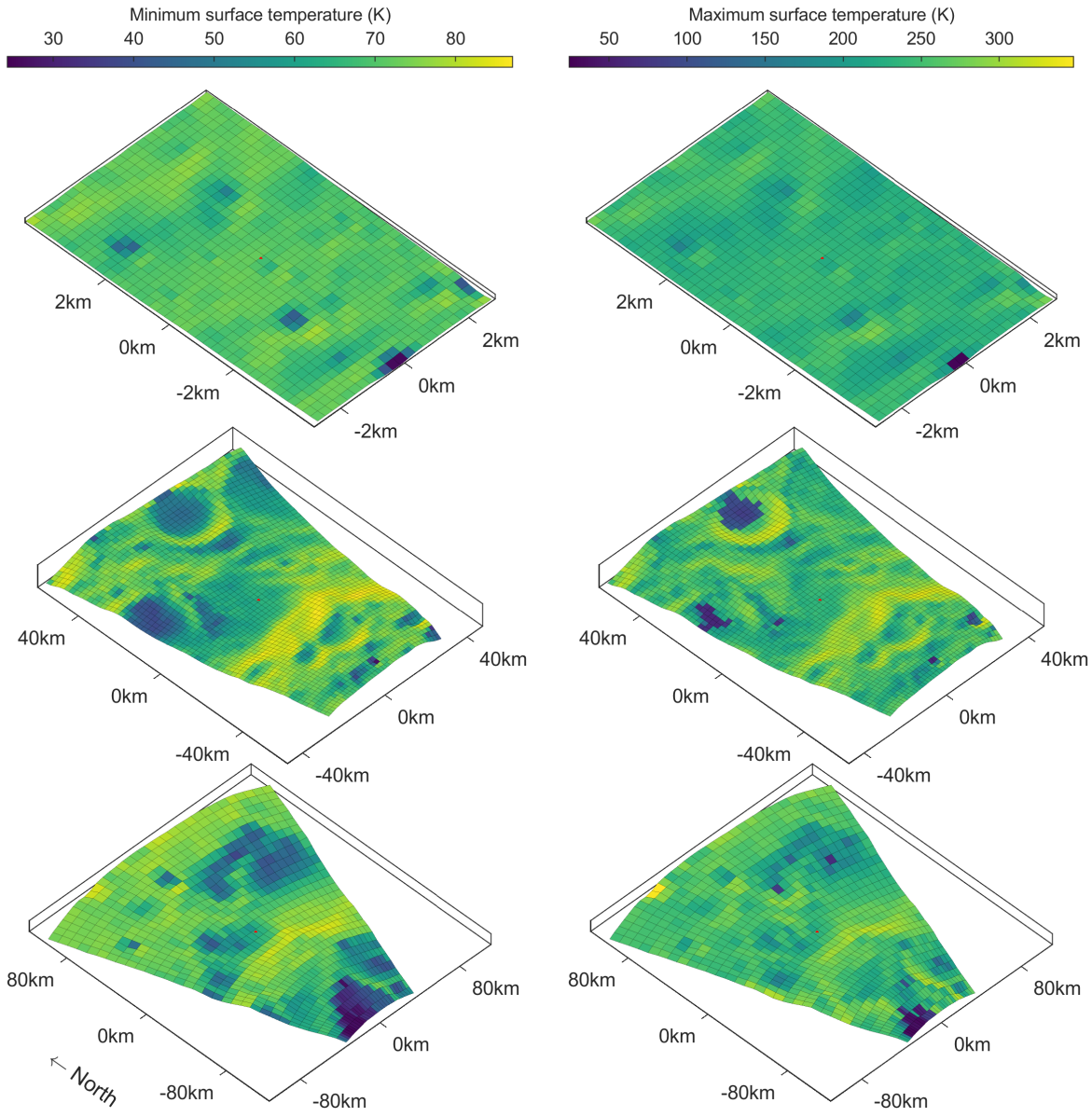

Figure 7: Modelled surface temperatures for different simulation environments around landing site 8. From top to bottom, plots are for 128ppd, 16ppd and 4ppd environments with minimum temperatures on the left and maximum temperatures on the right. The landing site location is given by the red dots.

7 Comparison to Diviner temperatures

In this section the modelled surface temperatures for each simulated landing site are compared to the measured Diviner bolometric temperatures. The measured temperatures are from the level 3 gridded Diviner dataset, which is on the same grid as the LOLA dataset, allowing easy comparison between the model and Diviner temperatures.

The temperatures are compared by calculating the 'average absolute error' and 'average error' for each surface element to identify regions which have various types of mismatch. The average absolute temperature error is defined as

$$\frac{1}{N}\sum_{i=1}^{N}\left(\left|T_{model}^{(i)} - T_{Diviner}^{(i)}\right|\right)$$

Equation 5

for each surface element, found by comparing the Diviner measurements $T_{Diviner}^{(i)}$ and corresponding modelled surface temperatures $T_{model}^{(i)}$ where N is the number of Diviner measurements for the surface element. This average absolute error is a measure of how consistently accurate the modelled temperature is. The average temperature error is defined as

$$\frac{1}{N}\sum_{i=1}^{N}\left(T_{model}^{(i)} - T_{Diviner}^{(i)}\right)$$

Equation 6

and is a measure of if the modelled temperature is systematically too warm or too cold. These errors are shown in Figure 8 for landing site 8.

In general, across all the simulations, the temperature errors are largest around sunrise and sunset, where the temperature is changing rapidly with time and the solar elevation is very low. During this period, errors in the model temperatures ($T_{model} - T_{Diviner}$) may be ~10 K due to a "timing error" where the model temperature changes slightly earlier or later than the Diviner temperature. This is likely to be due to the model only simulating the sun as a point source. The current implementation of the Sun as a point source causes the incident flux to change as a step function at the edge of a shadow. In reality the incidence flux should reduce gradually at the edge of a shadow (as there are parts of the surface where only part of the sun is visible). This will be improved in future versions of the model by representing the Sun as an extended source.

The "timing error" could also be due to the discrete simulation grid causing discrepancies in the calculated local solar incidence angle at low solar elevations.

The model accuracy is also low in regions that are in near permanent shadow, such as pole facing shallow slopes and surface elements on the boundary of permanently shaded regions. For many of these areas, the modelling of the sun as a point source and the discrete simulation grid causes the model to treat them as permanently shaded, even though they are only temporarily shadowed during the summer, leading to $T_{model}^{max} \ll T_{Diviner}^{max}$.

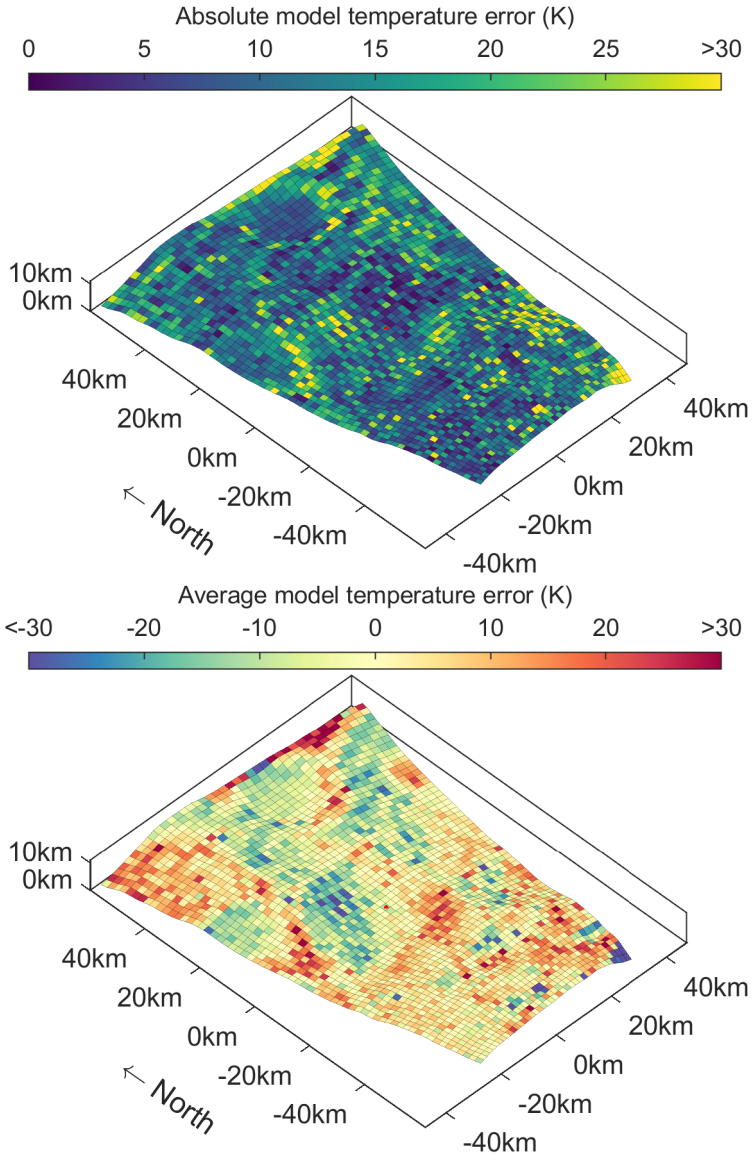

Figure 8: Error analysis of 3D thermal model at landing site 8. The top map shows the average absolute temperature error and the bottom map shows the average temperature error. The red dots show the location of landing site 8.

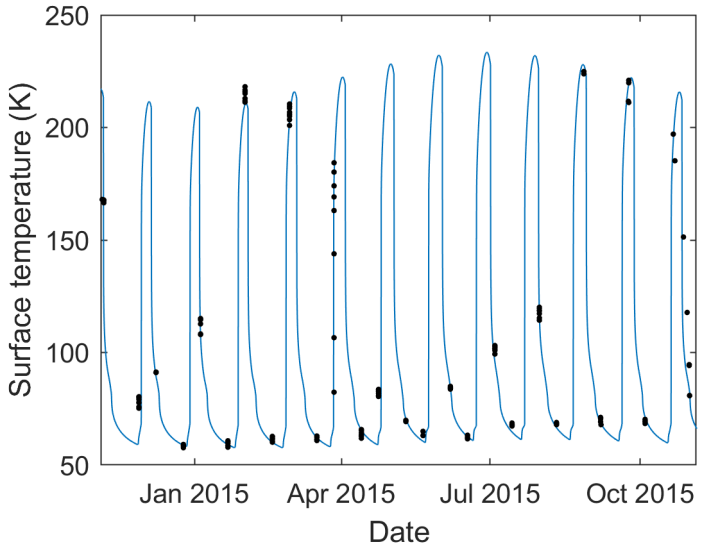

Figure 9: Comparison of model and diviner surface temperatures at landing site 8. The blue line is the modelled surface temperature and the black dots are Diviner measurements. There are multiple Diviner measurements at each time due to the simulation surface elements covering multiple Diviner pixels, so the model temperature should lie within the range of Diviner temperatures.

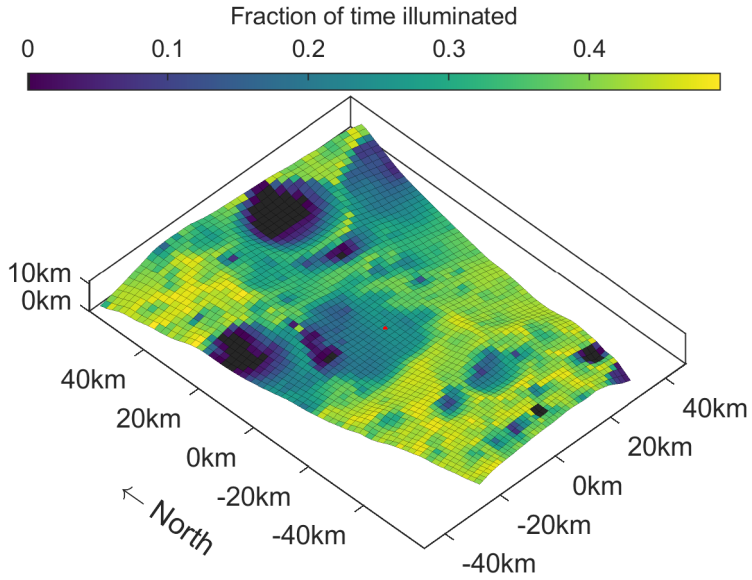

Figure 10: Illumination map for region surrounding landing site 8., calculated using ray tracing code used in the 3D model. Black regions are permanently shaded. The red dot shows the location of the landing site.

The model is less accurate for regions towards the edge of the simulated area. This is an expected result, as these regions will be much more affected by areas outside the simulated area than regions towards the centre of the simulated area. For example, the surface elements along the northern edge of the simulated area in Figure 8 are generally too warm in the model, as the terrain which shades them during part of the lunar day is not included in the simulation. The accuracy of the simulation at

the edge of the simulated area is therefore dependent on the local terrain – areas with steep slopes (e.g. craters and mountains) will be less accurate whereas a perfectly flat area would be accurate to the edge of the simulated area (due to the absence of mutual lines of sight between different parts of the surface).

8 Ice stability

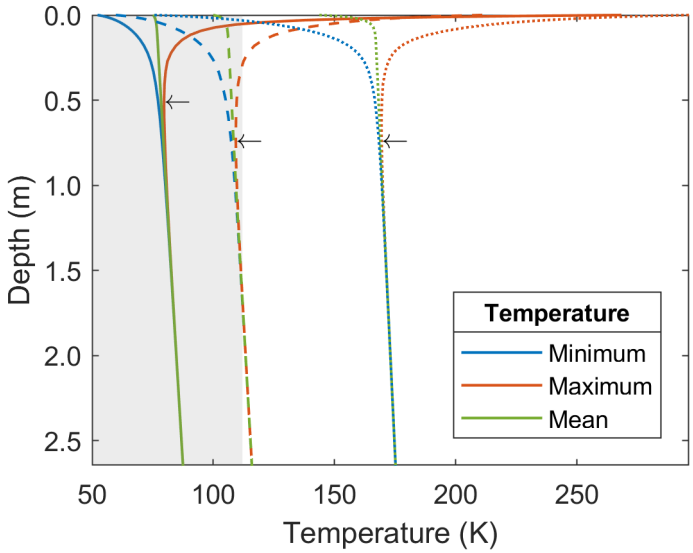

Figure 11: Sub-surface temperature profiles for simulated points near Landing Site 8. Ice is assumed to be stable for long periods of time at depths where the maximum temperature is less than 112 K, represented by the shaded area. The solid lines are a typical profile of an area where ice can be stable from a depth of 5 cm below the surface, the dashed lines are where ice can be stable from 29 cm to 167 cm below the surface and the dotted lines are a typical profile where ice cannot stable at any depth. The black arrows show the location of the minimum constant temperature for each profile. The large temperature variation near the surface is due to the diurnal temperature cycle, and the increase in temperature with depth is due to the lunar interior heat flux. Temperature values are from a year of simulation time (i.e. include a full seasonal cycle).

Ice stability is highly dependent on the temperature structure of the regolith. In this study, ice is assumed to be stable at a given depth if the temperature at that depth never exceeds 112 K (Paige et al, 1992). Therefore, it is possible for ice to be stable below the lunar surface at a given location if the "minimum constant temperature" of that location is <112 K. The minimum constant temperature of a surface element is defined to be the coldest maximum temperature of all the model layers for that surface element. For example, in Figure 11, the minimum constant temperature of the solid profile is 80 K, the dashed profile is 109 K and the dotted profile is 169 K (as indicated by the black arrows). This implies ice cannot be stable for the dotted profile as its minimum constant temperature is >112 K.

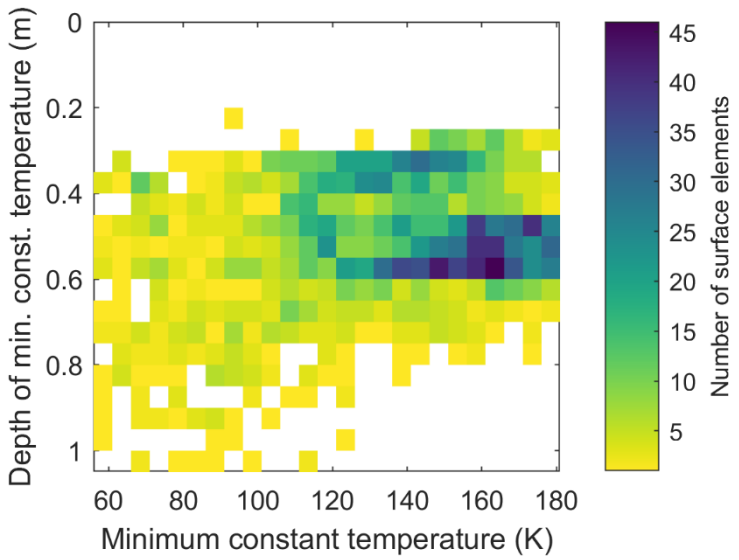

Figure 12: Relationship between simulated minimum constant temperature and its corresponding depth for the area surrounding landing site 8. White areas represent no surface elements.

The minimum constant temperature typically occurs at a depth of ~0.5 m (Figure 12). The depth of the minimum constant temperature varies slightly with the location – cold permanently shaded areas have shallower minimum constant temperatures due to the internal heat flux of the Moon dominating the temperature profile rather than surface heating (Figure 13). The modelled temperatures implicitly assume that the lunar surface consists of regolith-like material to depths >2.65 m. Therefore, the presence of any non-regolith subsurface material, such as bedrock, at these depths would significantly reduce the accuracy of the modelled temperatures and the ice stability inferred from them.

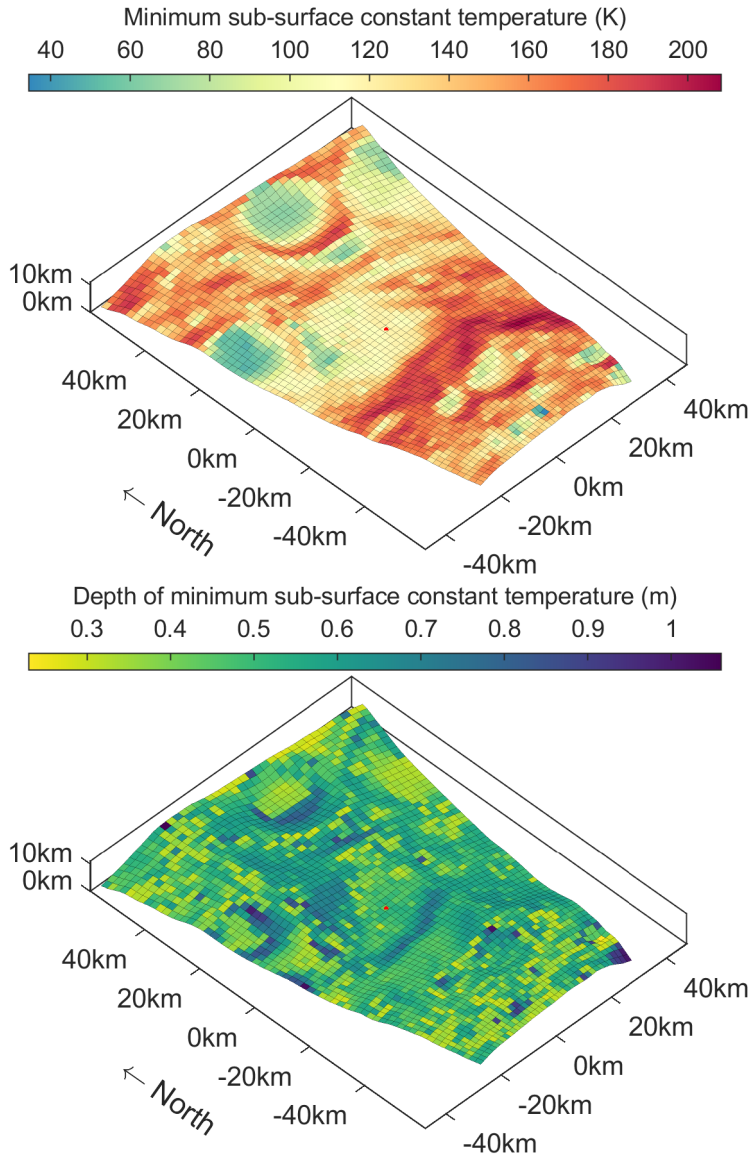

Figure 13: Minimum subsurface constant temperatures and corresponding depths for region surrounding of landing site 8. The red dots show the location of the landing site.

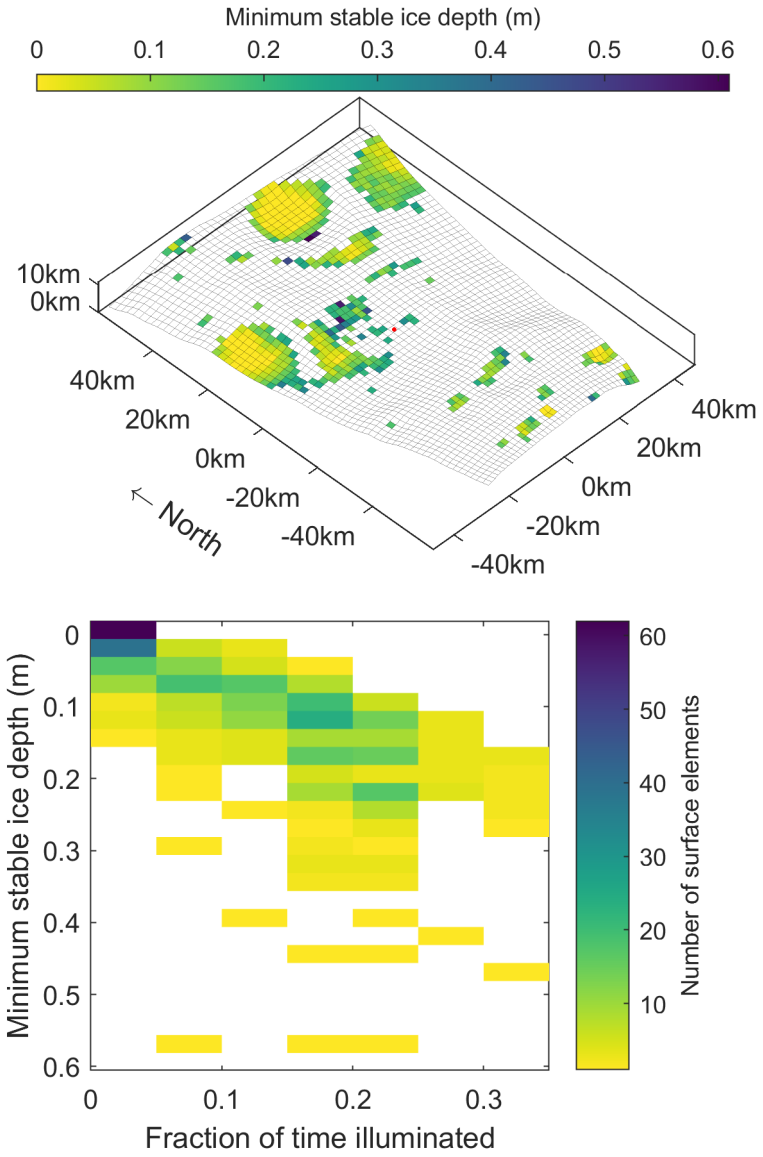

Figure 14: Simulated minimum stable depth of ice layer for landing site 8 (assuming ice is stable for a layer with a maximum temperature < 112 K). In the coldest, permanently shaded, areas ice can be stable at the surface. The graphs only show values for surface elements where ice can be stable. The red dot on the map shows the location of the landing site.

Figure 13 and Figure 14show the minimum sub-surface temperatures and therefore ice stability for the simulation of landing site 8. As expected, craters and pole-facing slopes are the coldest regions and are significantly below the 112 K required for long-term ice stability. This modelling work suggest the surface temperature in permanently shaded regions is usually cold enough to expect ice to be stable at the lunar surface. In more illuminated (>2.5% illumination time) regions ice can only be stable below the surface, as a layer of insulating regolith is required to keep the ice layer below 112 K during the day.

Across the model region surrounding site 8 the deepest minimum stable depth was found to be ~60 cm, consistent with the depth where the coldest constant temperatures generally occur (Figure 12). For surface elements where ice can be stable, the deepest stable layer is generally the bottom simulated layer, implying ice can be stable (T < 112 K) to large depths (much deeper than the 2.65 m simulated by the model). Ultimately, the internal heat flux of the moon will determine the depth of the bottom of the stable ice layer.

9 Conclusions

A new 3D thermal physical model (known as the Oxford 3D Thermal Physical Model) has been developed in MATLAB and is free to download along with example data outputs described in this paper (https://github.com/tw7044/O3DTM.git). The newly developed model combines the latest 1D thermal diffusion heat1d model (Hayne et al, 2017) with a 3D surface scattering model which was developed for this study. The new model is able to include non-lambertian scattering in both the thermal infrared and the visible. Although applied to the Moon in this study the Oxford 3D Thermal Physical Model can be applied to any airless body in the solar system.

For modelling the surface temperature of the lunar surface, the Oxford 3D Thermal Physical Model was found to be significantly more accurate than a 1D thermal model, at high latitudes and areas of strong terrain features where 3D (scattering and shadowing) effects are significant. In such regions a 1D model had typical errors of > 100 K, when compared to the measured surface bolometric temperatures from Diviner. A 3D model had typical errors in the same locations of ~10 K, when compared to the measured Diviner temperatures.

The main trade off with using a 3D model versus a 1D model is the long simulation times constraining the complexity and size of the model. Future studies with access to faster computers (or with more available time) will be able to carry out simulations on larger areas of the lunar surface and improve model complexity. The errors found with the 3D model suggest future model improvements should

focus on improving scattering calculations by including a bidirectional reflectance function and on modelling the Sun and each surface element as more than one point.

Modelling of study Luna27 landing sites near the lunar south pole identified two types of regions where ice can be stable. Permanently shaded regions are typically stable from the lunar surface down to large depths. Most illuminated regions are not generally stable at the surface (as brief periods of illumination in the summer heat the surface layer to > 112 K) but can have a layer of sub-surface ice stability. The coldest constant temperature typically occurs at a relatively shallow depth of ~50 cm and the minimum stable ice depth is also typically shallow <30 cm. These results show that, assuming careful selection of landing site the current design depth of the PROSPECT drill (~1 m) should be sufficient to sample trapped water ice.

The study sites modelling demonstrates to sample potential water deposits, it is more important to select your landing site accurately than to be able to drill deep. Most of the modelled regions surrounding the study sites did not contain any potential water ice at any depth and in the regions that did contain water ice the depth of expect water ice was relatively shallow. Therefore, the choice of landing site location and the precision landing capability of the lander are essential given the engineering constraints on the sampling system. There is an obvious correlation between the illumination fraction and the volatile stability conditions. Luna27/PROSPECT will therefore have a trade-off to select a site that will satisfy both critical power/operations requirements and science objectives of the PROSPECT mission.

10 Data Availability

All MATLAB code required run the O3DTM and data from the 8 sites described in this paper can be downloaded from https://github.com/tw7044/O3DTM.git.

11 Acknowledgements

The Authors would like to thank the European Space Agency (ESA), the United Kingdom Space Agency (UKSA), the Science and Technology Facilities Council (STFC) consolidated grant funding (ST/K00106X/1) and the Leverhulme Trust (RPG-2012-814) for supporting this work financially.

12 Bibliography

Bandfield, J.L., Hayne, P.O., Williams, J.P., Greenhagen, B.T. and Paige, D.A., 2015. Lunar surface roughness derived from LRO Diviner Radiometer observations. *Icarus*, 248, pp.357-372.

Braun, J.E. and Mitchell, J.C., 1983. Solar geometry for fixed and tracking surfaces. *Solar Energy, 31(*5), pp.439-444.

Carrier, W.D., 1973. Lunar soil grain size distribution. *The moon*, 6(3-4), pp.250-263.

Carslaw, H.S. and Jaeger, J.C., 1959. Conduction of heat in solids. *Oxford: Clarendon Press, 1959, 2nd ed*.

Foote, E.J., Paige, D.A., Johnson, J.R., Grundy, W.M. and Shepard, M.T., 2009, March. The bidirectional reflectance of Apollo 11 soil sample 10084. In *Lunar and Planetary Science Conference* (Vol. 40).

Fountain, J.A. and West, E.A., 1970. Thermal conductivity of particulate basalt as a function of density in simulated lunar and Martian environments. *Journal of Geophysical Research, 75*(20), pp.4063-4069.

Hayne, P., Bandfield, J., Vasavada, A., Ghent, R., Siegler, M., Williams, J.P., Greenhagen, B., Aharonson, O. and Paige, D., 2013, April. Thermophysical Properties of the Lunar Surface from Diviner Observations. In *EGU General Assembly Conference Abstracts* (Vol. 15).

Hayne, P.O., Bandfield, J.L., Siegler, M.A., Vasavada, A.R., Ghent, R.R., Williams, J.P., Greenhagen, B.T., Aharonson, O., Elder, C.M., Lucey, P.G. and Paige, D.A., 2017. Global regolith thermophysical

properties of the Moon from the Diviner Lunar Radiometer Experiment. *Journal of Geophysical Research: Planets*.

Hemingway, B.S., Krupka, K.M. and Robie, R.A., 1981. Heat capacities of the alkali feldspars between 350 and 1000 K from differential scanning calorimetry, the thermodynamic functions of the alkali feldspars from 298. 15 to 1400 K, and the reaction quartz+ jadeite= analbite. *Am. Mineral.;(United States), 66*.

Ingersoll, A.P., Svitek, T. and Murray, B.C., 1992. Stability of polar frosts in spherical bowl-shaped craters on the Moon, Mercury, and Mars. *Icarus, 100*(1), pp.40-47.

Jet Propulsion Laboratory. 2018. HORI- ZONS Web-Interface. Available at: http://ssd.jpl.nasa.gov/horizons.cgi. [Accessed 8 February 2018].

Keihm, S.J., 1984. Interpretation of the lunar mi- crowave brightness temperature spectrum: Feasibility of orbital heat flow mapping. *Icarus*, 60(3), pp.568-589

Kieffer, H.H., 2013. Thermal model for analysis of Mars infrared mapping. *Journal of Geophysical Research: Planets, 118*(3), pp.451-470.

Kopp, G. and Lean, J.L., 2011. A new, lower value of total solar irradiance: Evidence and cli- mate significance. *Geophysical Research Letters*, 38(1).

Lang, K.R., 2012. *Astrophysical data: Planets and stars*. Springer Science & Business Media.

Langseth, M.G., Keihm, S.J. and Peters, K., 1976, April. Revised lunar heat-flow values. In *Lunar and Planetary Science Conference Proceedings* (Vol. 7, pp. 3143-3171).

Ledlow, M.J., Zeilik, M., Burns, J.O., Gisler, G.R., Zhao, J.H. and Baker, D.N., 1992. Subsurface emissions from Mercury-VLA radio observations at 2 and 6 centimeters. *The Astrophysical Journal, 384*, pp.640-655.

587 Logan, L.M., Hunt, G.R., Balsamo, S.R. and Salisbury, J.W., 1972. Midinfrared emission spectra of
588 Apollo 14 and 15 soils and remote compositional mapping of the moon. In *Lunar and Planetary Science*
589 *Conference Proceedings* (Vol. 3, p. 3069).

590 Mitchell, D.L. and De Pater, I., 1994. Microwave imaging of Mercury's thermal emission at wavelengths
591 from 0.3 to 20.5 cm. *Icarus*, 110 (1), pp.2- 32.

592 Paige, D.A., Foote, M.C., Greenhagen, B.T., Schofield, J.T., Calcutt, S., Vasavada, A.R., Pre- ston, D.J.,
593 Taylor, F.W., Allen, C.C., Snook, K.J. and Jakosky, B.M., 2010a. The lunar recon- naissance orbiter
594 diviner lunar radiometer experiment. *Space Science Reviews*, 150(1-4), pp.125- 160.

595 Paige, D.A., Siegler, M.A., Zhang, J.A., Hayne, P.O., Foote, E.J., Bennett, K.A., Vasavada, A.R.,
596 Greenhagen, B.T., Schofield, J.T., McCleese, D.J. and Foote, M.C., 2010b. Diviner lunar radiometer
597 observations of cold traps in the Moons south polar region. *science*, 330(6003), pp.479-482.

598 Paige, D.A., Wood, S.E. and Vasavada, A.R., 1992. The thermal stability of water ice at the poles of
599 Mercury. *Science, 258*(5082), pp.643-646.

600 Pommerol, A., Thomas, N., Affolter, M., Portyankina, G., Jost, B., Seiferlin, K. and Aye, K.M., 2011.
601 Photometry and bulk physical properties of Solar System surfaces icy analogs: The Planetary Ice
602 Laboratory at University of Bern. *Planetary and space science*, 59(13), pp.1601- 1612.

603 Schorghofer, N. and Taylor, G.J., 2007. Subsurface migration of H2O at lunar cold traps. *Journal of*
604 *Geophysical Research: Planets, 112*(E2).

605 Sefton-Nash, E., Williams, J.P., Bandfield, J., Warren, T., Greenhagen, B. and Paige, D., 2018,
606 September. Far-IR Emissivity in Lunar South Polar Permanently Shaded Terrain: Apparent
607 Temperature Dependence. In *European Planetary Science Congress* (Vol. 12).

608 Siegler, M.A. and Feng, J., 2017, March. Microwave remote sensing of lunar subsurface temperatures:
609 reconciling Chang'e MRM and LRO diviner. In *Lunar and Planetary Science Conference* (Vol. 48).

610 Smith, D.E., Zuber, M.T., Jackson, G.B., Cavanaugh, J.F., Neumann, G.A., Riris, H., Sun, X., Zellar, R.S.,
611 Coltharp, C., Connelly, J. and Katz, R.B., 2010. The lunar orbiter laser altimeter investigation on the
612 lunar reconnaissance or- biter mission. *Space science reviews, 150*(1-4), pp.209-241.

613 Vasavada, A.R., Bandfield, J.L., Greenhagen, B.T., Hayne, P.O., Siegler, M.A., Williams, J.P. and Paige,
614 D.A., 2012. Lunar equatorial surface temperatures and regolith properties from the Diviner Lunar
615 Radiometer Experiment. *Journal of Geophysical Research: Planets, 117*(E12).

616 Vasavada, A.R., Paige, D.A. and Wood, S.E., 1999. Near-surface temperatures on Mercury and the
617 Moon and the stability of polar ice deposits. *Icarus*, 141(2), pp.179-193.

618 Wang, Z., Li, Y., Zhang, D., Jiang, J., Zhao, J., Hua, F. and Zhang, X., 2010, May. Prelaunch calibration of
619 Chang'E-2 Lunar Microwave radiometer. In *2010 International Conference on Microwave and*
620 *Millimeter Wave Technology* (pp. 1551-1554). IEEE.

621 Warren, T.J., Bowles, N.E., Donaldson Hanna, K. and Thomas, I.R., 2017. The Oxford space environment
622 goniometer: A new experimental setup for making directional emissivity measurements under a
623 simulated space environment. *Review of Scientific Instruments*, *88*(12), p.124502.

624 Warren, T.J., Bowles, N.E., Donaldson Hanna, K. and Bandfield, J.L., 2019. Modeling the angular
625 dependence of emissivity of randomly rough surfaces. *Journal of Geophysical Research: Planets*,
626 *124*(2), pp.585-601.

627 Wei, G., Li, X. and Wang, S., 2016. Inversions of subsurface temperature and thermal diffusivity on the
628 Moon based on high frequency of Chang'E-1 microwave radiometer data. *Icarus*, *275*, pp.97-106.

629 Whipple, F.L., 1950. A comet model. I. The acceleration of Comet Encke. *The Astrophysical Journal*,
630 111, pp.375-394.

631 Zhang, J.A. and Paige, D.A., 2009. Cold-trapped organic compounds at the poles of the Moon and
632 Mercury: Implications for origins. *Geophysical Research Letters*, *36*(16).